



In situ growth of the δ -manganese dioxide on carbon cloth by different concentrations of reactants for eco-friendly battery applications

Yaping Feng¹ · Youfeng Zhang¹ · Yichen Zhang¹ · Liang Zhang² · Yinling Wang²

Received: 5 April 2023 / Revised: 7 June 2023 / Accepted: 11 June 2023 / Published online: 20 June 2023
© The Author(s), under exclusive licence to Springer-Verlag GmbH Germany, part of Springer Nature 2023

Abstract

Aqueous zinc ion batteries (AZIBs) have drawn more notice because of their affordability, high security, and favorable ecological impact. So far, manganese oxide (MnO_2) is thought to be an attractive material for storing energy among cathodes of aqueous zinc ion batteries. In particular, the layered manganese dioxide (δ - MnO_2) is more favorable to the diffusion of ions and can provide higher specific capacity. However, The effect of the concentration of reactants on microstructure and electrochemical performance of δ - MnO_2 , which has been less studied. Herein, the δ - MnO_2 deposited on carbon fabric as the cathodes of AZIBs by four different reactant concentrations (0.05 M, 0.07 M, 0.10 M, and 0.12 M) of potassium permanganate solution were successfully prepared. The electrochemical properties of AZIBs fabricated by reactant concentrations of 0.10 M KMnO_4 were excellent. The δ - MnO_2/CC -0.10 M cathode provided higher rechargeable capacity of $268 \text{ mA h} \cdot \text{g}^{-1}$ at $0.1 \text{ A} \cdot \text{g}^{-1}$, outstanding rate capability, and long cycle life of 97.3% preservation after 500 cycles at $2 \text{ A} \cdot \text{g}^{-1}$. This study systematically demonstrates the influence of reagent concentration on the efficiency and stability of aqueous zinc–manganese ion batteries.

Keywords δ - MnO_2 nanosheets · Potassium permanganate · Aqueous zinc ion batteries · Hydrothermal method · Carbon cloth

Introduction

Nowadays, the continued use of fossil fuels, energy scarcity, and climate change have become global concerns [1–3]. Therefore, people are concerned about renewable clean energy. To make better use of this renewable clean energy, efficient energy conversion and storage systems are essential [4, 5]. Battery energy storage technology realizes the storage and utilization of energy through the mutual conversion between chemical energy and electric energy. It not only promotes the widespread use of electric vehicles and reduces dependence on fossil energy, but is also an effective solution

for the large-scale reuse of intermittent renewable energy [6–10]. Lithium-ion batteries (LIBs) are the most prevalent power storage units used with light rechargeable electronics owing to their low density and good cycle stability [11–14]. Wei et al. developed a slurry flow battery with an extended potential window, excellent redox stability, and strong fluidity by dispersing small-sized lithium-storage active material particles and conductive agents into high-salinity aqueous electrolytes, which has a coulomb efficiency close to 100%, long cycle life, and high safety. It has numerous applications in the world of energy storage [15]. The troubles of high price, heavy pollution, low safety, and scarcity of lithium metal resources are becoming increasingly prominent with the continuous expansion of the lithium-ion battery manufacturing industry [11], so researchers begin to seek effective alternative technologies for LIBs. For example, the aqueous redox flow batteries (ARFBs) are the promising grid-scale energy storage system that uses redox active molecules dissolved in non-combustible aqueous solution as the electrolyte [16–18]. Furthermore, aqueous zinc ion batteries (AZIBs) are seen as a possible substitute for LIBs because of their great safety and less expensiveness [19]. AZIBs mostly use aqueous solution containing zinc salt as

✉ Youfeng Zhang
zhangyoufeng@sues.edu.cn

✉ Liang Zhang
zhangliang0202@163.com

¹ School of Materials Science and Engineering, Shanghai University of Engineering Science, Shanghai 201620, People's Republic of China

² Henan Engineering Laboratory of New Energy Conversion and Control Technology, Huanghuai University, Zhumadian, Henan 463000, People's Republic of China

electrolyte, which is more affordable, safer, and more sustainable than the organic electrolyte. What's more, compared to organic electrolytes, the aqueous electrolyte has a much greater conductivity and can dissolve electrolyte compounds with higher concentrations [20, 21]. These characteristics make AZIBs have a wide prospect in application.

For AZIBs, the radius of Zn^{2+} (0.74 Å) is close to Li^+ (0.76 Å), which means that most of the materials used in LIBs can also be used for AZIBs. Wei et al. used the combination of the excluded volume electrolyte HBCD and the organic DC-PDESA cathode to achieve a high open circuit voltage (1.7 V), a wide operating temperature range ($-20 \sim 90$ °C), excellent rate capability, and long cycle life for zinc ion batteries (the capacity retention is 98.3% after 2000 cycles), which achieve high safety and low cost energy storage system applications [22]. Transition metal oxides, especially manganese dioxide, are suitable as cathode materials for AZIBs because of their inexpensiveness and low toxicity [23–28]. The crystal forms of manganese dioxide include α , β , γ , δ , λ , and R [29]. It is worth noting that δ - MnO_2 holds a unique lamellar structure with a layer distance of roughly 0.7 nm [30, 31], which facilitates the diffusion of Zn^{2+} between the layers, implying that δ - MnO_2 has better electrochemical performance and energy storage capacity. The layered WSe_2 nano-flower as cathode materials for zinc ion batteries was synthesized by a simple solvent method. It has been discovered that the layered structure is beneficial to improve the specific surface area and conductivity of the electrode material, and thus, the WSe_2 cathode material has high discharge specific capacity, excellent rate performance, and cycle stability [32]. Researchers have made many attempts to enhance the cycling efficiency and rate capability for MnO_2 electrode materials. Ma et al. implanted Cu ions into δ - MnO_2 to promote the electrochemical properties of AZIBs and obtained laminated $\text{Cu}@\delta$ - MnO_2 with large storage capacity, superior cycling behavior, and rate capacity [33]. Liao et al. produced β - MnO_2 /ppy composite through a hydrothermal process. Under the current density of 0.2 A g^{-1} , its discharge capacitance is 361.8 mAh g^{-1} , and its rate performance is better than that of pure MnO_2 [34]. Deng et al. prepared β - MnO_2 @CC on carbon fiber fabric. It completely contacts the electrolyte since the significant area of specific surface and the inside surface of β - MnO_2 are tightly coupled to the conductive carbon fiber fabric, showing excellent electrochemical performance [35]. Besides, the influence of reagent concentration on the microstructure and electrochemical properties of cathode materials in AZIBs has been studied less. The concentration of KMnO_4 which affected the electrochemical behaviors and structure characteristics of MnO_2 for the supercapacitor was explored by Han et al. It was found that the MnO_2 -4.5

has stable capacitance and high discharge efficiency [36]. ZnMn_2O_4 nanoparticles doped with Ni^{2+} were prepared by Qin et al. and used as cathode materials for AZIBs. It was discovered the ZMO/Ni-3 had a larger capacitance and superior charge and discharge reversibility. After activation, the electrode demonstrates a capacity of 175 mAh g^{-1} at 0.1 A g^{-1} . It can still retain 120 mAhg^{-1} under a high current density of 1 A g^{-1} and maintain a coulomb efficiency of more than 97% throughout the cycle, with the exception of the first cycle [37]. Li et al. discovered that in sodium-ion batteries, reagent concentration and aging time regulated play a critical part in the morphology and behaviors of electrode materials and that optimal reagent concentration and precipitation time result in the best grain size with a stable monoclinic structure, relatively few defects, and regular cubic morphology [38]. Zampardi et al. synthesized different powders of CuHCF based on different concentrations of $\text{Cu}(\text{NO}_3)_2$ and $\text{K}_3\text{Fe}(\text{CN})_6$ in a zinc ion battery. Although there was no discernible alteration to the morphology of CuHCF powder, the difference in elemental potassium content changed the lattice bond distance, which affected the cycling durability and stability of the electrode material [39]. Furthermore, the improved electrochemical properties of cathode may also be attributed to the inhibition of Mn dissolution [40]. The electrochemical properties of the AZIBs are significantly increased by adding Mn^{2+} to the electrolyte to prevent Mn from dissolving [41, 42]. The above research can improve the cycle performance and rate efficiency in some degree, but the factor of reactant concentration on the microstructure and electrical characteristics of cathode materials in AZIBs has been studied less.

In this research, the δ - MnO_2 /CC cathodes were prepared by hydrothermal synthesis with varying concentrations of reactants for AZIBs. The obtained δ - MnO_2 /CC was tested for composition, morphological characterization, and electrochemical performances. The findings demonstrate that the concentration of KMnO_4 has a great impact on it, which is extremely crucial in the application of MnO_2 .

Experimental section

Materials

Potassium permanganate (KMnO_4 , 99.5%) was purchased from Shanghai Titan Technology Co., Ltd., China. The carbon cloth (CC) (WOS1011, 0.36 mm thickness) was purchased from a company of Taiwan carbon energy and Zn foil (99.98%, 0.20 mm in thickness) was purchased from Cyber Electrochemical Materials Network.

Pretreatment of CC

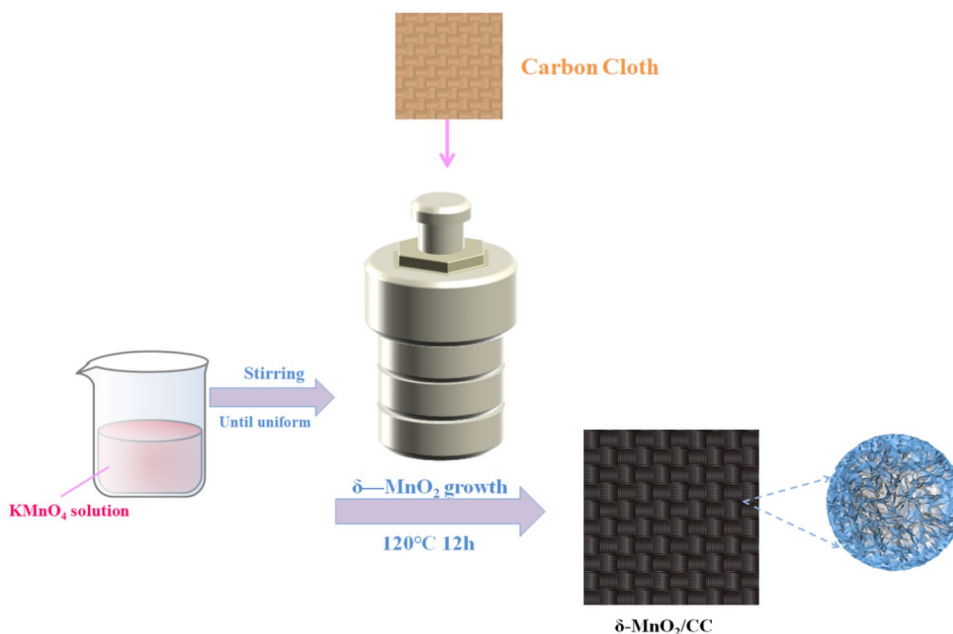
The carbon cloth was cut into a square of 2 cm × 2 cm squares and placed in a Teflon liner with a mixture of 69 mL HNO₃ and 17 mL distilled water, put into the oven, and reacted at 120 °C for 24 h. After the reaction, it was washed several times with distilled water and ethanol until the PH reached 7, and then dried in the oven.

Preparation of δ-MnO₂/CC cathode

Firstly, KMnO₄ was dissolved in 30 mL of distilled water at concentrations of 0.05 M, 0.07 M, 0.10 M, and 0.12 M, respectively labeled as solutions I, II, III, and IV under constant magnetic stirring for about 3 h, and moved to Teflon-lined stainless steel autoclave liners. Secondly, CC was affixed to a glass slide and immersed in the solution, and kept at 120°C for 12 h before being cooled to ambient temperature. After the process, the dark brown product-coated carbon cloth was taken out of the autoclave and given 2–3 washes in distilled water and alcohol. Lastly, δ-MnO₂/CC cathode material was obtained by drying at 70 °C for 6 h, as depicted in Fig. 1. Besides, the photos of bare CC substrate and δ-MnO₂/CC are present in Fig. S1a. Additionally, the four samples are designated as δ-MnO₂/CC-0.05 M, δ-MnO₂/CC-0.07 M, δ-MnO₂/CC-0.10 M, and δ-MnO₂/CC-0.12 M, and the oxidation–reduction reaction is represented by the following formula [43]:



Fig. 1 The schematic of primary preparation method and electrode morphology of δ-MnO₂ nanosheets on CC



Assembly of button batteries

AZIBs could be built directly in an open laboratory; the cathode was made by shearing the δ-MnO₂/CC material into a 1 cm × 1 cm square. The anode was composed of Zn metal foil with a thickness of 0.20 mm. The electrolyte is aqueous solution of 2 M ZnSO₄ with 0.2 M MnSO₄ added to prevent MnO₂ from dissolving, glass fiber as the separator. Besides, the battery was assembled using stainless steel gaskets, stainless steel shrapnel, and CR2032 positive and negative battery shells.

Structural characterization

X-ray diffraction (XRD, Ultima IV, Rigaku, Japan) using Cu Kα radiation was taken to analyze the phase structure. The surface morphologies and the lattice fringe of samples were investigated using scanning electron microscopy (SEM, Gemini 300) and transmission electron microscopy (TEM, JEOL 2100F). The elemental composition and mapping of the samples were determined using elemental-dispersive X-ray spectroscopy (EDS). X-ray photoelectron spectroscopy (XPS, Thermo Scientific K-Alpha) was used to examine the surface chemical valence and molecular structure. The surface area of the Brunauer–Emmett–Teller (BET) was assessed to use nitrogen adsorption/desorption on an ASAP2460 instrument.

Electrochemical tests

The δ-MnO₂/CC specimens were straightly served as the test electrode, and no adhesive or conductive additive is added.

The CV curve was measured at a scan rate of 0.1 mV s^{-1} in the voltage range of 1–1.8 V vs. Zn^{2+}/Zn by the AUTO LAB electrochemical workstation. Battery Test System (NEWARE, Neware Co. Ltd., China) was applied to test the electrochemical charging and discharging behavior from 1.0 to 1.8 V vs. Zn^{2+}/Zn at normal temperature. Electrochemical impedance spectroscopy (EIS) was surveyed at frequencies between 0.01 Hz and 100 kHz using the electrochemical workstation (CorrTest).

Results and discussion

Figure 2a depicts the XRD spectrums of $\delta\text{-MnO}_2/\text{CC}$. The image displays four main peaks at 12.5° , 25.2° , 37.3° , and 66.2° , which have the space group C2/m (JCPDS No. 80–1098) and can be assigned to the (001), (002), ($\bar{1}11$), and (005) planes of birnessite MnO_2 [44]. The interlayer distance between (001) crystal planes is about 0.709 nm [45]. The XRD results show that the film formed on carbon fiber cloth is $\delta\text{-MnO}_2$ without any other MnO_x formed. The binding energy of atoms and the detailed elemental composition of the samples were examined using X-ray photoelectron spectroscopy (XPS) in order to confirm the elemental valence of MnO_2/CC . The full spectrum characteristic peak of MnO_2/CC can be seen in Fig. 2b. It can be found that the sample mainly comprises the components Mn, O, and

C. Figure 2c displays the bond energies of Mn 2p_{3/2} and Mn 2p_{1/2} are 642.18 eV and 653.67 eV, respectively. The binding separation is 11.49 eV, which verified the existence of MnO_2 [46]. The XPS spectra of O1s in Fig. 2d contained three dominant peaks, corresponding to the Mn–O–Mn bonds (529.5 eV), Mn–O–H bonds (531.3 eV), and H–O–H bonds (532.9 eV), respectively [47]. The results of XPS analysis confirmed that the substance was MnO_2 , which agrees with the XRD result.

The morphologies and mapping of the cathode materials were examined by SEM and TEM. Figure 3a1–d2 show the surface microstructure of $\delta\text{-MnO}_2/\text{CC}$ at low and high amplification. It can be seen from Fig. 3a1–c1 that the $\delta\text{-MnO}_2/\text{CC}$ generated by different reactant concentrations are nanospheres composed of nanosheets, indicating that the reactant concentration has little effect on the morphology of $\delta\text{-MnO}_2/\text{CC}$. These nanosheets are connected with each other to form spaces and pores [48], which not only facilitate ion transport and electrolyte diffusion [49], but also alleviate the variation of volume of the material during Zn^{2+} storage. It is visible that there are some holes in the $\delta\text{-MnO}_2/\text{CC}$ -0.10 M (Fig. 3c2, black section) after the nanospheres have been amplified further, and the size is large and evenly distributed. This characteristic promotes ion movement in the electrode material, and the structure is difficult to collapse. There are fewer and smaller internal pores in the $\delta\text{-MnO}_2/\text{CC}$ -0.05 M and $\delta\text{-MnO}_2/\text{CC}$ -0.12 M in Fig. 3a2

Fig. 2 a XRD spectrums. b XPS survey pattern. c Mn 2p. d O 1s

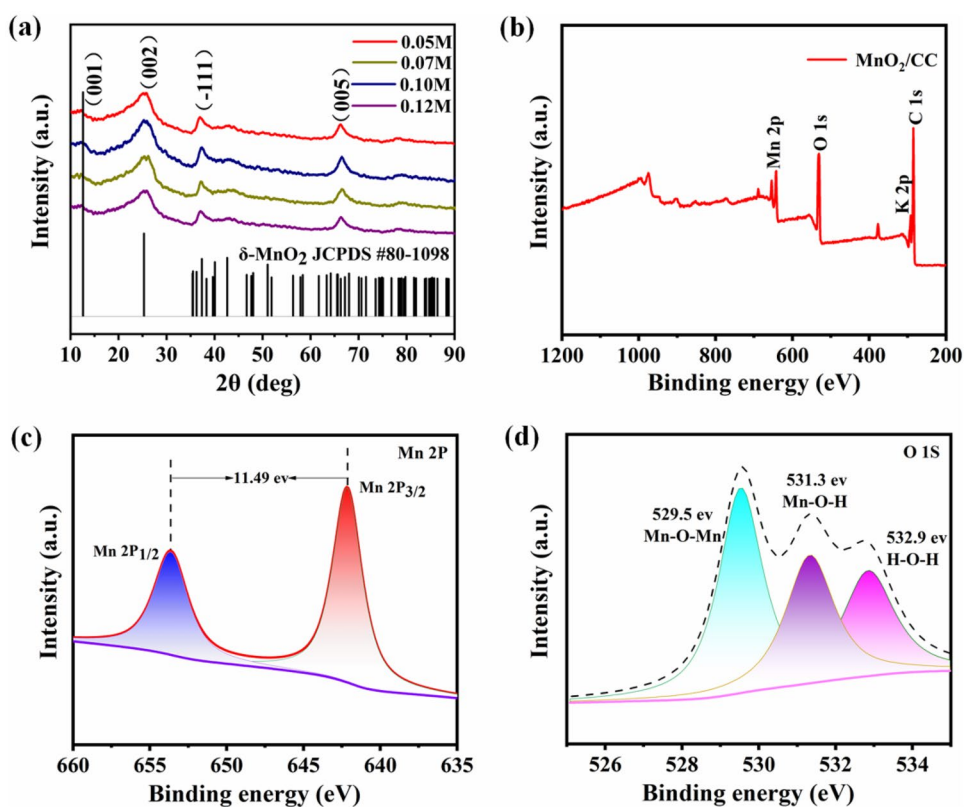
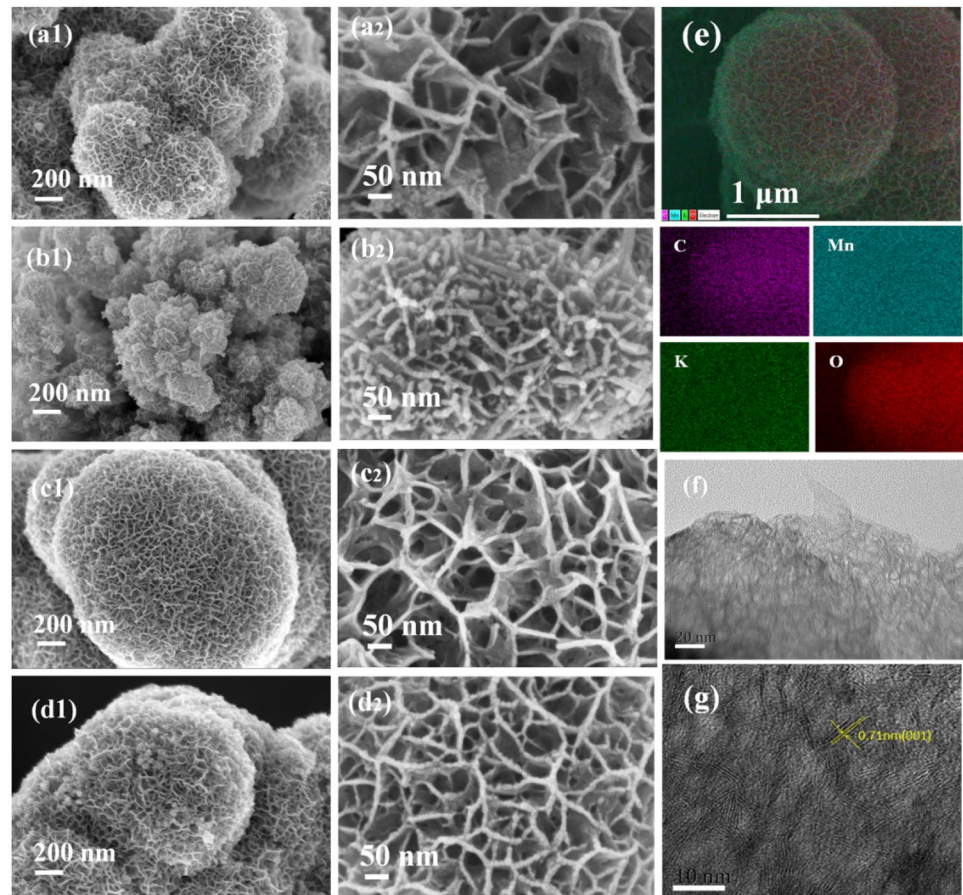


Fig. 3 SEM images of δ -MnO₂/CC. **a1, a2** δ -MnO₂/CC-0.05 M. **b1, b2** δ -MnO₂/CC-0.07 M. **c1, c2** δ -MnO₂/CC-0.10 M. **d1, d2** δ -MnO₂/CC-0.12 M. **e** EDS images of the δ -MnO₂/CC-0.10 M. **f** TEM images of δ -MnO₂/CC-0.10 M. **g** HRTEM images of δ -MnO₂/CC-0.10 M



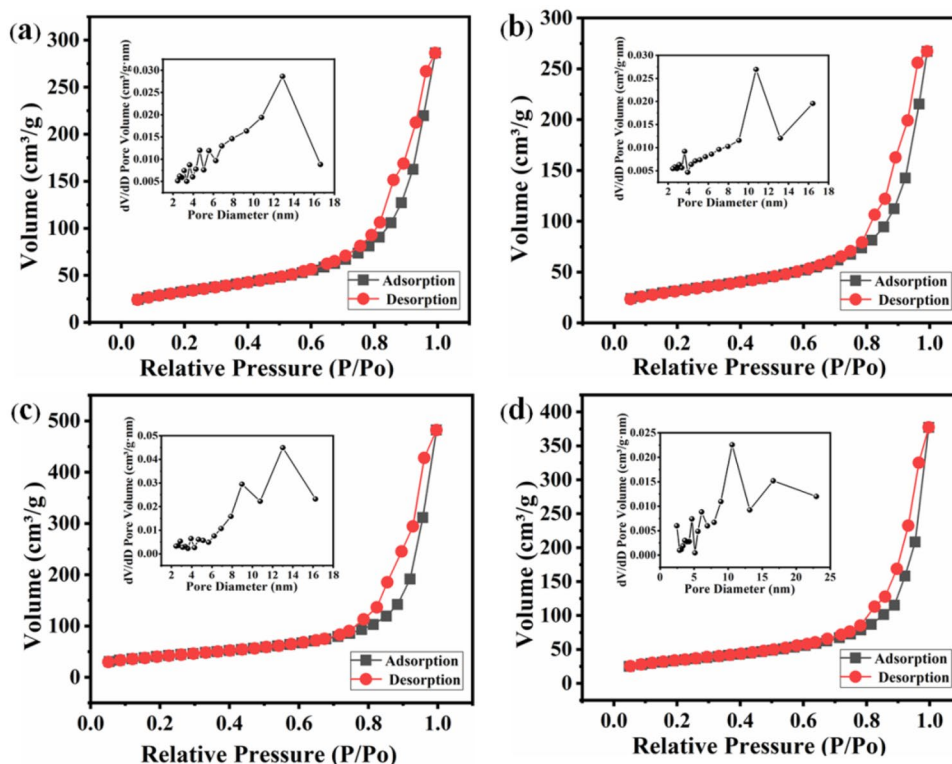
and d2. The surface pores of δ -MnO₂/CC-0.07 M in Fig. 3b2 are almost absent, and the ion transport pathways are too narrow for ion transport, which led to the electrochemical performance to reduce.

Figure S1b, c show the sample δ -MnO₂/CC-0.10 M nanosheets growing uniformly on carbon cloth, which confirms that the concentration of 0.10 M has a better morphology. The EDS mapping analysis of Fig. 3e demonstrates that the elements of O (red), Mn (blue), K (green), and C (purple) are uniformly distributed, which further suggests that the synthesis of δ -MnO₂/CC was successful. Furthermore, Fig. S2 demonstrates the percentage content of each element, and proves that MnO₂/CC is the main substance. More elaborated information about structure and morphology of δ -MnO₂/CC was supplied by TEM. The thin nanosheet morphology of sample δ -MnO₂/CC-0.10 M is evident in Fig. 3f. The HRTEM images of the corresponding δ -MnO₂/CC-0.10 M in Fig. 3g show that the lattice stripe spacing of 0.71 nm matches with the (001) plane spacing of δ -MnO₂, which indicates that the MnO₂ cathode layer is well crystallized. This layered structure is conducive to the movement of charged particles in the crystal lattice, resulting in oxidation–reduction reaction or ion exchange, and will not cause the destruction of the layered structure of the crystal.

Figure 4 shows the BET surface area for δ -MnO₂/CC hybrids. The subsequent of the BET surface areas for the four compounds is as follows: δ -MnO₂/CC-0.10 M (146.98 m² g⁻¹) > δ -MnO₂/CC-0.12 M (110.62 m² g⁻¹) > δ -MnO₂/CC-0.05 M (110.60 m² g⁻¹) > δ -MnO₂/CC-0.07 M (104.12 m² g⁻¹). It can be seen from Fig. 3c2 and d2 that, at the same magnification, δ -MnO₂/CC-0.10 M has more mesoporous distribution than δ -MnO₂/CC-0.12 M. Furthermore, the internal pores of δ -MnO₂/CC-0.10 M are more than those of δ -MnO₂/CC-0.12 M. The four samples demonstrate the type IV isotherms according to IUPAC recommendation, which indicates mesoporous structure [50, 51]. As shown in the insets of Fig. 4, these four materials show analogous apertures between 2 and 8 nm. The mesoporous structure is instrumental in the full electrode-to-electrolyte contact, which is convenient for the electrolyte to access the space of the electrode material to store charges, so as to obtain better electrochemical performance [52].

Remarkable electrochemical behavior of AZIB is a significant indicator of their proper preparation. Figure 5a exhibits the CV results at a sweep rate of 0.1 mV s⁻¹ from 1.0 to 1.8 V. Two separate anodic and cathodic peaks of δ -MnO₂/CC electrode occur around 1.6 V and 1.35 V during cycling, respectively. The presence of cathodic peak is attributed to

Fig. 4 N_2 adsorption–desorption isotherm of δ - MnO_2/CC hybrids. **a** δ - MnO_2/CC -0.05 M. **b** δ - MnO_2/CC -0.07 M. **c** δ - MnO_2/CC -0.10 M. **d** δ - MnO_2/CC -0.12 M. The distributions of pore size plots are depicted in the inset images



Zn^{2+} intercalation into MnO_2 and Mn^{4+} which is reduced to the low valence state. Correspondingly, the appearance of anodic peak is owed to Zn^{2+} de-intercalation out of MnO_2 and the oxidation of Mn from low valence state to Mn^{4+} [53], $xZn^{2+} + 2xe^- + MnO_2 \leftrightarrow Zn_xMnO_2$. In comparison to δ - MnO_2/CC -0.05 M, δ - MnO_2/CC -0.07 M, and δ - MnO_2/CC -0.12 M electrodes, it is noticeable that the δ - MnO_2/CC -0.10 M electrode has a bigger region of CV curves and a stronger current response, indicating superior capacity performance. The redox peaks of the δ - MnO_2/CC -0.10 M have a much lower potential difference than those of the other compounds.

It demonstrates the outstanding electrochemical inevitability of the δ - MnO_2/CC -0.10 M cathode material [54]. The representative CV findings of the δ - MnO_2/CC -0.10 M

cathode existed in the voltage window of 1.0–1.8 V at various sweep rates in Fig. 5b, which proves that the highly reversible redox reaction is present in this cell reaction, implying that the δ - MnO_2/CC -0.10 M cathode is stable [55]. Meanwhile, the shape of the CV plot of the δ - MnO_2/CC -0.10 M cathode remains similar under multiple scan rates, indicating that the charge was transported rapidly in the electrode. The polarization effect causes the peak positions of the cathode and anode to shift towards the negative and positive potentials as the scan rate increases [56].

The electrochemical properties of the prepared AZIB were thoroughly investigated, and the findings are displayed in Fig. 6. Figure 6a depicts the galvanostatic discharge/charge curves measured from 1.0 to 1.8 V under $0.1A\ g^{-1}$. The discharge capacities of δ - MnO_2/CC -0.05 M,

Fig. 5 **a** CV curves of δ - MnO_2/CC at a scan rate of 0.1 mV/s. **b** CV curves of the δ - MnO_2/CC -0.10 M at different scan rates

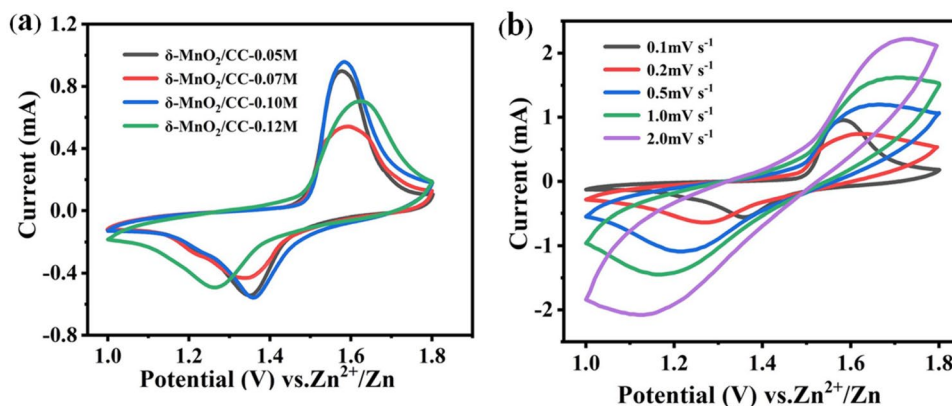
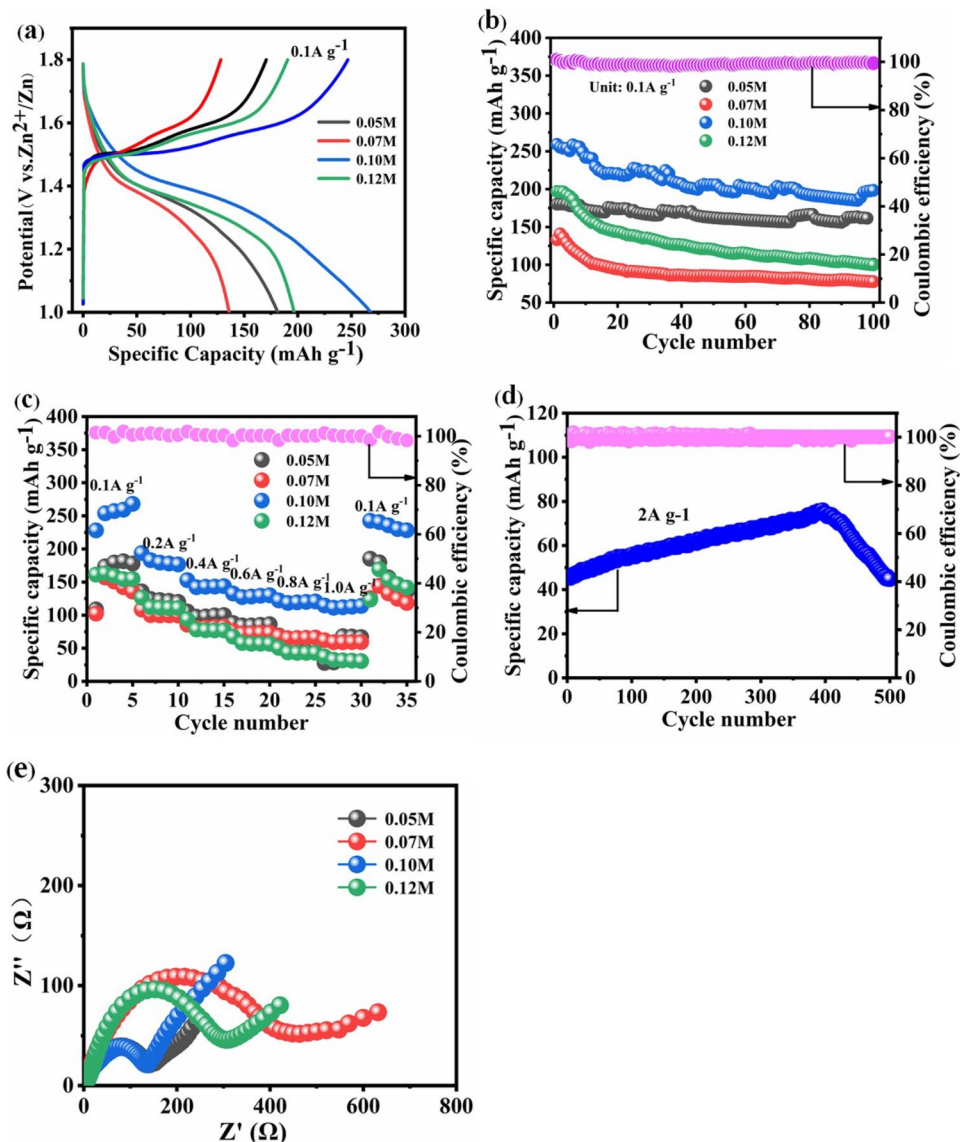


Fig. 6 **a** Charge and discharge curves of $\delta\text{-MnO}_2/\text{CC}$ at 0.1 A g^{-1} for the first cycle. **b** Cycling behavior of $\delta\text{-MnO}_2/\text{CC}$ at 0.1 A g^{-1} . **c** Rate performance of $\delta\text{-MnO}_2/\text{CC}$. **d** Cycling performance of the $\delta\text{-MnO}_2/\text{CC}-0.10\text{ M}$ at 2.0 A g^{-1} for 500 cycles. **e** Electrochemical impedance spectroscopy (EIS) curves of the $\delta\text{-MnO}_2/\text{CC}$ electrodes



$\delta\text{-MnO}_2/\text{CC}-0.07\text{ M}$, and $\delta\text{-MnO}_2/\text{CC}-0.12\text{ M}$ are 181 mAh g^{-1} , 136 mAh g^{-1} , and 196 mAh g^{-1} , respectively. The $\delta\text{-MnO}_2/\text{CC}-0.10\text{ M}$ displays a high discharge capacitance of 268 mAh g^{-1} at 0.1 A g^{-1} , which is greater than those of $\delta\text{-MnO}_2/\text{CC}-0.05\text{ M}$, $\delta\text{-MnO}_2/\text{CC}-0.07\text{ M}$, and $\delta\text{-MnO}_2/\text{CC}-0.12\text{ M}$. It mainly benefits from the large specific surface area of the $\delta\text{-MnO}_2/\text{CC}-0.10\text{ M}$ electrode material, which ensures sufficient contact between the active material and the electrolyte, and thus reduces the impedance of the electrode. Besides, the $\delta\text{-MnO}_2/\text{CC}-0.10\text{ M}$ charge–discharge platform has the smallest voltage difference, indicating the lower polarization and better charging performance [54, 57]. Besides, the cycling behavior of the AZIB with $\delta\text{-MnO}_2/\text{CC}$ is displayed in Fig. 6b, which demonstrates the cathode of the $\delta\text{-MnO}_2/\text{CC}-0.10\text{ M}$ has excellent circulation stability with capacitance of about 198 mAh g^{-1} at 0.1 A g^{-1} after 100 cycles, which has a high Coulombic efficiency (CE)

of 99.87%. The large electrode/electrolyte touch region can be provided by the large surface area and high porousness of $\delta\text{-MnO}_2/\text{CC}-0.10\text{ M}$, which can also be conducive to the diffusion of Zn^{2+} ions. Hence, it has better electrochemical properties [58]. Figure S3 displays SEM images of $\delta\text{-MnO}_2/\text{CC}$ electrode after 100 cycles. The surface of the electrode material exhibits the phenomenon of nanosheet collapse after 100 charge–discharge cycles, yet it retains its original morphology overall. This observation suggests that the structure remains stable and the battery cycle performance is excellent. The $\delta\text{-MnO}_2/\text{CC}-0.07\text{ M}$ sample contains many small particles. According to research, when the particle size is too small, the interface between the particles increases, resulting in insufficient contact with the electrolyte and poor cycling performance of the AZIBs [59]. The CE dropped to 98.95% compared to $\delta\text{-MnO}_2/\text{CC}-0.10\text{ M}$. Additionally, the Coulombic efficiencies of $\delta\text{-MnO}_2/\text{CC}-0.05\text{ M}$ and $\delta\text{-MnO}_2/\text{CC}-0.12\text{ M}$

CC-0.12 M are 99.33% and 99.19%, respectively. Figure 6c presents the rate capacity for the products of δ -MnO₂/CC at different current rates of 0.1 A g⁻¹, 0.2 A g⁻¹, 0.4 A g⁻¹, 0.6 A g⁻¹, 0.8 A g⁻¹, and 1.0 A g⁻¹. The δ -MnO₂/CC-0.10 M cathode shows the reversible capacities of 268, 194, 153, 132, 122, and 114 mAh g⁻¹, respectively. The advantage of δ -MnO₂/CC-0.10 M electrode is that a large number of diffusion channels are provided by the uniform distribution and large size of pores for zinc ions, while ensuring the full infiltration of the electrolyte, improving the rate performance of the battery. This is superior to the other three groups of samples. After several cycles with different high current densities, when the current density is restored to 0.1 A g⁻¹, the AZIB discharge specific capacitance remains 243 mAh g⁻¹ (91% of capacity retention). It can be observed that the Coulombic efficiency of δ -MnO₂/CC-0.10 M is the highest. Surprisingly, the Coulombic efficiency of δ -MnO₂/CC-0.05 M, δ -MnO₂/CC-0.07 M, and δ -MnO₂/CC-0.12 M is 99.25%, 99.35%, and 99.73%, respectively. It fully shows that the δ -MnO₂/CC still maintains excellent reversibility at high current density.

The long-life cycle ability and Coulombic effectiveness of the δ -MnO₂/CC-0.10 M at 2.0 A g⁻¹ are evaluated in Fig. 6d. The activation of electrode materials and the gradual penetration of electrolyte may be responsible for the rise in specific capacity during cycling. As the cycle increases, the process of zinc ion embedding in the electrode material slows down, leading to a decrease in specific capacity. The phenomenon that the specific capacity of the electrode increases first and then decreases during the charge and discharge process of Zn-Mn batteries is common [14, 60–62]. The AZIB could still maintain 97.3% of first capacity after 500 cycles, and high Coulombic effectiveness, indicating the outstanding cycling stability of the AZIB. This is mostly attributable to the large pore volume of the δ -MnO₂/CC-0.10 M, which is beneficial to the transfer of Zn²⁺ and the infiltration of electrolyte, and can still have excellent capacity retention after multiple cycles. Figure 6e exhibits the electrochemical impedance spectroscopy (EIS). Charge transfer resistance is reflected by the semi-round diameter of the high frequency. As can be seen from Fig. 6e, compared to δ -MnO₂/CC-0.07 M and δ -MnO₂/CC-0.12 M, the charge transport resistor of δ -MnO₂/CC-0.10 M is significantly reduced, but slightly lower than that of δ -MnO₂/CC-0.05 M, which indicates that δ -MnO₂/CC-0.10 M has high conductivity. Moreover, the slope of δ -MnO₂/CC-0.10 M in the low-frequency region is greater than those of δ -MnO₂/CC-0.05 M, δ -MnO₂/CC-0.07 M, and δ -MnO₂/CC-0.12 M, indicating that the diffusion rate of zinc ions in δ -MnO₂/CC-0.10 M is higher [62]. This corresponds to the higher initial capacitance of δ -MnO₂/CC-0.10 M in the cyclic test.

Conclusion

In short, the layered structure of δ -MnO₂/CC is prepared by a simple one-step hydrothermal method. The impacts of KMnO₄ concentration on the electrochemical properties of δ -MnO₂/CC were studied. In contrast to δ -MnO₂/CC-0.05 M, δ -MnO₂/CC-0.07 M, and δ -MnO₂/CC-0.12 M, the δ -MnO₂/CC-0.10 M possesses a greater surface area (146.98 m² g⁻¹), which supplies sufficient active sites and reduces the ion migration range, leading to exhibit excellent electrochemical properties (specific capacity of 268 mAh g⁻¹ at 0.1 A g⁻¹) and long-time durability (97.3% capacity retention for 500 cycles at 2.0 A g⁻¹ and Coulombic efficiency close to 100%), high reversibility, and excellent rate performance. These results provide ideas for further progress of electrodes with cost-effectiveness, high capacitance, and high safety for integrated structure batteries.

Supplementary Information The online version contains supplementary material available at <https://doi.org/10.1007/s10008-023-05569-9>.

Acknowledgements This work was supported by the Class III Peak Discipline of Shanghai-Materials Science and Engineering (High-Energy Beam Intelligent Processing and Green Manufacturing).

References

1. Davies DM, Verde MG, Mnyshenko O, Chen YR, Rajeev R, Meng YS, Elliott G (2018) Combined economic and technological evaluation of battery energy storage for grid applications. *Nat Energy* 4:42–50
2. Larcher D, Tarascon JM (2015) Towards greener and more sustainable batteries for electrical energy storage. *Nat Chem* 7:19–29
3. Zhang Y, He S, Zhang Y, Feng Y, Pan Z, Zhang M (2022) Facile synthesis of PPy@MoS₂ hollow microtubes for removal of cationic and anionic dyes in water treatment. *Colloids Surf A Physicochem Eng Aspects* 632:127765
4. Seregin VV, Finkelman RB (2008) Metalliferous coals: a review of the main genetic and geochemical types. *Int J Coal Geol* 76:253–289
5. Tian X, Lu XF, Xia BY, Lou XW (2020) Advanced electrocatalysts for the oxygen reduction reaction in energy conversion technologies. *Joule* 4:45–68
6. Armand M, Tarascon J-M (2008) Building better batteries. *Nature* 451:652–657
7. Ji X (2019) A paradigm of storage batteries. *Energ Environ Sci* 12:3203–3224
8. Dunn B, Kamath H, Tarascon J-M (2011) Electrical energy storage for the grid: a battery of choices. *Science* 334:928–935
9. Soloveichik GL (2011) Battery technologies for large-scale stationary energy storage. *Annu Rev Chem Biomol Eng* 2:503–527
10. Liu J, Hu J, Deng Q, Mo J, Xie H, Liu Z, Xiong Y, Wu X, Wu Y (2015) Aqueous rechargeable batteries for large-scale energy storage. *Isr J Chem* 55:521–536
11. Etacheri V, Marom R, Elazari R, Salitra G, Aurbach D (2011) Challenges in the development of advanced Li-ion batteries: a review. *Energ Environ Sci* 4:3243–3262

12. Liu G, Wang N, Qi F, Lu X, Liang Y, Sun Z (2023) Novel Ni-Ge-P anodes for lithium-ion batteries with enhanced reversibility and reduced redox potential. *Inorg Chem Front* 10:699–711
13. Liang Y, Chen Y, Ke X, Zhang Z, Wu W, Lin G, Zhou Z, Shi Z (2020) Coupling of triporosity and strong Au–Li interaction to enable dendrite-free lithium plating/stripping for long-life lithium metal anodes. *J Mater Chem A* 8:18094–18105
14. Liu G, Yang Y, Lu X, Qi F, Liang Y, Trukhanov A, Wu Y, Sun Z, Lu X (2022) Fully active bimetallic phosphide Zn(0.5)Ge(0.5)P: a novel high-performance anode for Na-ion batteries coupled with diglyme-based electrolyte. *ACS Appl Mater Interfaces* 14:31803–31813
15. Wei J, Zhang P, Liu Y, Liang J, Xia Y, Tao A, Zhang K, Tie Z, Jin Z (2022) Hypersaline aqueous lithium-ion slurry flow batteries. *ACS Energy Lett* 7:862–870
16. Liu Y, Wen G-H, Liang J, Bao S-S, Wei J, Wang H, Zhang P, Zhu M, Jia Q, Ma J, Zheng L-M, Jin Z (2022) Aqueous colloid flow batteries based on redox-reversible polyoxometalate clusters and size-exclusive membranes. *ACS Energy Lett* 8:387–397
17. Wang C, Yu B, Liu Y, Wang H, Zhang Z, Xie C, Li X, Zhang H, Jin Z (2021) N-Alkyl-carboxylate-functionalized anthraquinone for long-cycling aqueous redox flow batteries. *Energy Storage Mater* 36:417–426
18. Pan M, Shao M, Jin Z (2023) Development of organic redox-active materials in aqueous flow batteries: current strategies and future perspectives. *SmartMat* e1198
19. Kim C, Phillips PJ, Key B, Yi T, Nordlund D, Yu YS, Bayliss RD, Han SD, He M, Zhang Z, Burrell AK, Klie RF, Cabana J (2015) Direct observation of reversible magnesium ion intercalation into a spinel oxide host. *Adv Mater* 27:3377–3384
20. Kundu D, Adams BD, Duffort V, Vajargah SH, Nazar LF (2016) A high-capacity and long-life aqueous rechargeable zinc battery using a metal oxide intercalation cathode. *Nat Energy* 1:16119
21. Huang S, Zhu J, Tian J, Niu Z (2019) Recent progress in the electrolytes of aqueous zinc-ion batteries. *Chemistry* 25:14480–14494
22. Wei J, Zhang P, Shen T, Liu Y, Dai T, Tie Z, Jin Z (2022) Supramolecule-based excluded-volume electrolytes and conjugated sulfonamide cathodes for high-voltage and long-cycling aqueous zinc-ion batteries. *ACS Energy Lett* 8:762–771
23. Mathew V, Lim J, Kang J, Gim J, Rai AK, Kim J (2011) Self-assembled mesoporous manganese oxide with high surface area by ambient temperature synthesis and its enhanced electrochemical properties. *Electrochem Commun* 13:730–733
24. Jiao F, Bruce PG (2007) Mesoporous crystalline β -MnO₂—a reversible positive electrode for rechargeable lithium batteries. *Adv Mater* 19:657–660
25. Dai J, Li SFY, Siow KS, Gao Z (2000) Synthesis and characterization of the hollandite-type MnO₂ as a cathode material in lithium batteries. *Electrochim Acta* 45:2211–2217
26. Hashem AM, Abdel-Latif AM, Abuzeid HM, Abbas HM, Ehrenberg H, Farag RS, Mauger A, Julien CM (2011) Improvement of the electrochemical performance of nanosized α -MnO₂ used as cathode material for Li-batteries by Sn-doping. *J Alloys Compd* 509:9669–9674
27. Hill LI, Verbaere A, Guyomard D (2003) MnO₂ (α -, β -, γ -) compounds prepared by hydrothermal-electrochemical synthesis: characterization, morphology, and lithium insertion behavior. *J Power Sources* 119–121:226–231
28. Devaraj S, Munichandraiah N (2008) Effect of crystallographic structure of MnO₂ on its electrochemical capacitance properties. *J Phys Chem C* 112:4406–4417
29. Jia X, Liu C, Neale ZG, Yang J, Cao G (2020) Active materials for aqueous zinc ion batteries: synthesis, crystal structure, morphology, and electrochemistry. *Chem Rev* 120:7795–7866
30. Komaba S, Kumagai N, Chiba S (2000) Synthesis of layered MnO₂ by calcination of KMnO₄ for rechargeable lithium battery cathode. *Electrochim Acta* 46:31–37
31. Matsuo Y, Miyamoto Y, Fukutsuka T, Sugie Y (2005) Cathode properties of birnessite type manganese oxide prepared by using vanadium xerogel. *J Power Sources* 146:300–303
32. Hu J, Li J, Wei Z, Zhang S (2022) High-energy aqueous rechargeable batteries based on WSe₂ nano-flower cathode. *J Solid State Electr* 26:1605–1612
33. Ma S-M, Wang T-X, Deng Z-Y, Zheng X-S, Wang B-B, Feng H-J (2022) Improved performance of Cu ion implanted δ -MnO₂ cathode material for aqueous Zn-ion batteries. *Phys Lett A* 451:128400
34. Liao X, Pan C, Pan Y, Yin C (2021) Synthesis of three-dimensional β -MnO₂/PPy composite for high-performance cathode in zinc-ion batteries. *J Alloys Compd* 888:161619
35. Deng Z, Huang J, Liu J, Ren L, Zhu L, Xiao X, Tan M (2019) β -MnO₂ nanolayer coated on carbon cloth as a high-activity aqueous zinc-ion battery cathode with high-capacity and long-cycle-life. *Mater Lett* 248:207–210
36. Han R, Xing S, Ma Z, Wu Y, Gao Y (2012) Effect of the KMnO₄ concentration on the structure and electrochemical behavior of MnO₂. *J Mater Sci* 47:3822–3827
37. Qin L, Zhu Q, Li L, Cheng H, Li W, Fang Z, Mo M, Chen S (2023) Ni²⁺-doped ZnMn₂O₄ with enhanced electrochemical performance as cathode material for aqueous zinc-ion batteries. *J Solid State Electr* 27:773–784
38. Li Y, Lam KH, Hou X (2021) Reactant concentration and aging-time-regulated potassium manganese hexacyanoferrate as a superior cathode for sodium-ion batteries. *ACS Appl Energy Mater* 4:13098–13109
39. Zampardi G, Warnecke M, Tribbia M, Glenneberg J, Santos C, La Mantia F (2021) Effect of the reactants concentration on the synthesis and cycle life of copper hexacyanoferrate for aqueous Zn-ion batteries. *Electrochem Commun* 126:107030
40. Wu B, Zhang G, Yan M, Xiong T, He P, He L, Xu X, Mai L (2018) Graphene scroll-coated α -MnO₂ nanowires as high-performance cathode materials for aqueous Zn-ion battery. *Small* 14:1703850
41. Pan H, Shao Y, Yan P, Cheng Y, Han KS, Nie Z, Wang C, Yang J, Li X, Bhattacharya P, Mueller KT, Liu J (2016) Reversible aqueous zinc/manganese oxide energy storage from conversion reactions. *Nat Energy* 1:16039
42. Siamionau UV, Aniskevich YM, Ragoisha GA, Streltsov EA (2023) MnO₂ electrodeposition at the positive electrode of zinc-ion aqueous battery containing Zn²⁺ and Mn²⁺ cations. *J Solid State Electr*
43. Guo D, Yu X, Shi W, Luo Y, Li Q, Wang T (2014) Facile synthesis of well-ordered manganese oxide nanosheet arrays on carbon cloth for high-performance supercapacitors. *J Mater Chem A* 2:8833
44. Xia H, Lai M, Lu L (2010) Nanoflaky MnO₂/carbon nanotube nanocomposites as anode materials for lithium-ion batteries. *J Mater Chem* 20:6896–6902
45. Zhao G, Li J, Jiang L, Dong H, Wang X, Hu W (2012) Synthesizing MnO₂ nanosheets from graphene oxide templates for high performance pseudosupercapacitors. *Chem Sci* 3:433–437
46. Mathur A, Kaushik R, Halder A (2021) Photoenhanced performance of cobalt-intercalated 2-D manganese oxide sheets for rechargeable zinc–air batteries. *Mater Today Energy* 19:100612
47. Yang L, Cheng S, Wang J, Ji X, Jiang Y, Yao M, Wu P, Wang M, Zhou J, Liu M (2016) Investigation into the origin of high stability of δ -MnO₂ pseudo-capacitive electrode using operando Raman spectroscopy. *Nano Energy* 30:293–302
48. Zhang Y, He S, He Z, Zhang Y, Feng Y, Wang Y, Zhang M (2022) Preparation of MoS₂ and MoO₃ modified TiO₂ composites with

- enhanced visible-light photocatalytic activity for dye degradation. *Int J Electrochem Sci* 17:220210
49. Gao X, Zang W, Li X, Wang Z, Zheng L, Kou Z (2023) Achieving efficient alkaline hydrogen evolution reaction on long-range Ni sites in Ru clusters-immobilized Ni₃N array catalyst. *Chem Eng J* 451:138698
 50. Xia A, Yu W, Yi J, Tan G, Ren H, Liu C (2019) Synthesis of porous δ-MnO₂ nanosheets and their supercapacitor performance. *J Electroanal Chem* 839:25–31
 51. He S, Zhang Y, Ren J, Wang B, Zhang Z, Zhang M (2020) Facile synthesis of TiO₂@MoS₂ hollow microtubes for removal of organic pollutants in water treatment. *Colloids Surf A Physicochem Eng Aspects* 600:124900
 52. Zou F, Hu X, Li Z, Qie L, Hu C, Zeng R, Jiang Y, Huang Y (2014) MOF-derived porous ZnO/ZnFe₂O₄/C octahedra with hollow interiors for high-rate lithium-ion batteries. *Adv Mater* 26:6622–6628
 53. Wei C, Xu C, Li B, Du H, Kang F (2012) Preparation and characterization of manganese dioxides with nano-sized tunnel structures for zinc ion storage. *J Phys Chem Solids* 73:1487–1491
 54. Xue Y, Wang Z-B, Zheng L-L, Yu F-D, Liu B-S, Zhang Y, Zhou Y-X (2015) Synthesis and performance of hollow LiNi_{0.5}Mn_{1.5}O₄ with different particle sizes for lithium-ion batteries. *RSC Adv* 5:100730–100735
 55. Shao Z, Cheng S, Zhang Y, Guo H, Cui X, Sun Z, Liu Y, Wu Y, Cui P, Fu J, Su Q, Xie E (2021) Wearable and fully biocompatible all-in-one structured “paper-like” zinc ion battery. *ACS Appl Mater Interfaces* 13:34349–34356
 56. Zhang H, Lu C, Hou H, Ma Y, Yuan S (2019) Facile morphology-controlled synthesis of Co₃O₄ nanostructure on carbon cloth and their morphology-dependent pseudocapacitive performances. *J Alloys Compd* 797:970–977
 57. Kataoka F, Ishida T, Nagita K, Kumbhar V, Yamabuki K, Nakayama M (2020) Cobalt-doped layered MnO₂ thin film electrochemically grown on nitrogen-doped carbon cloth for aqueous zinc-ion batteries. *ACS Appl Energy Mater* 3:4720–4726
 58. Qin X, Zhou M, Zong B, Guo J, Gong J, Wang L, Liang G (2018) Urea-assisted hydrothermal synthesis of a hollow hierarchical LiNi_{0.5}Mn_{1.5}O₄ cathode material with tunable morphology characteristics. *RSC Adv* 8:30087–30097
 59. Xue Y, Wang Z-B, Zheng L-L, Yu F-D, Liu B-S, Zhou Y-X (2017) Investigation on spinel LiNi_{0.5}Mn_{1.5}O₄ synthesized by MnCO₃ prepared under different conditions for lithium-ion batteries. *ChemistrySelect* 2:4325–4331
 60. Zeng S, Song Y, Shi X, Xu W, Zheng D, Wang F, Xu C, Lu X (2022) Crystal form modulation enables high-performance manganese dioxide cathode for aqueous zinc ion battery. *J Alloys Compd* 913
 61. Ruan P, Xu X, Gao X, Feng J, Yu L, Cai Y, Gao X, Shi W, Wu F, Liu W, Zang X, Ma F, Cao X (2021) Achieving long-cycle-life Zn-ion batteries through interfacial engineering of MnO₂-polyaniline hybrid networks. *Sustain Mater Technol* 28
 62. Wu F, Gao X, Xu X, Jiang Y, Gao X, Yin R, Shi W, Liu W, Lu G, Cao X (2020) Boosted Zn storage performance of MnO₂ nanosheet-assembled hollow polyhedron grown on carbon cloth via a facile wet chemical synthesis. *Chemsuschem* 13:1537–1545

Publisher's Note Springer Nature remains neutral with regard to jurisdictional claims in published maps and institutional affiliations.

Springer Nature or its licensor (e.g. a society or other partner) holds exclusive rights to this article under a publishing agreement with the author(s) or other rightsholder(s); author self-archiving of the accepted manuscript version of this article is solely governed by the terms of such publishing agreement and applicable law.